Article

Not peer-reviewed version

Geochemistry and Mineralogy of the Clay-Type Ni-Laterite Deposit of San Felipe (Camagüey, Cuba)

Esperança Tauler *, Salvador Galí *, Cristina Villanova de Benavent *, Alfonso Chang-Rodriguez *, Kenia Nuñez-Cambra *, Giorgi Khazaradze *, Joaquin Antonio Proenza *

Posted Date: 4 August 2023

doi: 10.20944/preprints202308.0428.v1

Keywords: weathering; laterite; nickel; smectite; serpentine; clay-type; Cuba

Article

Geochemistry and Mineralogy of the Clay-Type Ni-Laterite Deposit of San Felipe (Camagüey, Cuba)

Esperança Tauler [1,*], Salvador Galí [1], Cristina Villanova-de-Benavent [1], Alfonso Chang-Rodríguez [2], Kenya Núñez-Cambra [3], Giorgi Khazaradze [1] and Joaquín A. Proenza [1]

[1] Departament de Mineralogia, Petrologia i Geologia Aplicada, Facultat de Ciències de la Terra, Universitat de Barcelona (UB), Martí i Franquès 1, 08028 Barcelona, Catalunya, Spain. esperancatauler@ub.edu; gali@ub.edu; cvillanovadb@ub.edu; gkhazar@ub.edu; japroenza@ub.edu

[2] Empresa Geominera Camagüey, Carretera Central Este Km51/2. Camagüey, Cuba. chang@reduc.edu.cu

[3] Instituto de Geología y Paleontología de Cuba, Vía Blanca, Línea del Ferrocarril s/n, San Miguel del Padrón, Habana 10200, Cuba. kenya@igp.minem.cu

* Correspondence: esperancatauler@ub.edu

Abstract: The Ni-laterite deposit at the San Felipe plateau, located 30 km northwest of Camagüey, in central Cuba, is the best example of a clay-type deposit in the Caribbean region. San Felipe resulted from weathering of mantle peridotites of the Cretaceous Camagüey ophiolites. In this study, a geochemical and mineralogical characterization of two profiles (83 and 84) from the San Felipe deposit has been performed by XRF, ICP-MS, quantitative XRPD, oriented aggregate mount XRD, SEM, FE-SEM and EMPA. Core 83 with a length of 23 m, and drilled in the central part of the plateau, presents a notable concentration of cryptocrystalline quartz fragments and a rather poor content in NiO, averaging 0.87% wt. Core 84, which is 12 m long, and drilled at the border of the plateau, lacks silica fragments and presents a higher NiO content, averaging 1.79 %wt. The smectite structural formulae reveal that they evolve from trioctahedral to dioctahedral towards the top of the laterite profiles. Quantitative XRD analyses indicate that smectite is a dominant Ni bearing phase, accompanied by serpentine and minor chlorite. Serpentine, as smectite, is enriched in the less soluble elements Fe^{3+}, Al and Ni towards the top of the profiles. Core 83 seems to have been affected by collapses, replenishments, whereas core 84 may have remained undisturbed.

Keywords: weathering; laterite; nickel; smectite; serpentine; clay-type; Cuba

1. Introduction

Nickel laterites are regolith materials derived from the chemical weathering of ultramafic rocks that contain economically exploitable reserves of Ni, as well as Co (e.g., [1] and references therein) and Sc [2,3]. Ni-laterites represent 70% of the world's Ni reserves, and 60% of the world's current production [4,5]. These deposits develop in humid climates during periods of low tectonic activity and in areas of moderate relief [1]. There are many factors that may control the specific structure of each lateritic profile [6–12]. However, the general structure of the profile is determined by the mobility of the different elements which are released by hydrolysis of primary (and secondary) minerals. This structure consists broadly of a silicate-bearing saprolite horizon near the ultramafic protolith, topped by an oxide zone, separated by the so-called magnesium discontinuity [11]. There are different classifications of nickel laterites depending on the morphology, lithology of the bedrock, degree of weathering, etc. [13,14]; although the most used one establishes three types of deposits according to the mineralogy of the dominant ore [15]. The main hosts of Ni are iron oxyhydroxides, concentrated in the oxide zone, in the oxide-type Ni-laterites; Ni-serpentine and garnierite, found in the saprolite horizon of hydrous Mg silicate-type Ni-laterites; and smectites in clay-type Ni-laterites. A particularity of clay-type Ni-laterite deposits is that the Ni-bearing smectites are concentrated in a transition zone between the saprolite horizon and the oxide zone [15].

 doi:10.20944/preprints202308.0428.v1

Detailed mineralogical studies have been carried out in numerous hydrous Mg silicate-type Ni-laterites (e.g., [8,16–19]). Oxide type Ni-laterites (e.g., [2,20]) and clay-type Ni-laterites (e.g., [9,21–23]) are far less common worldwide. Besides, other deposits can be described as a mixture of clay-type and hydrous Mg silicate-type ([23,24].

The San Felipe lateritic nickel deposit (Cuba) represents the best example of a clay-type Ni-laterite deposit in the Caribbean region, with current resources of 250 Mt at 1.43 % Ni, 0.05 % Co [25]. Unfortunately, limited data on the San Felipe deposit exists, and mostly in Spanish (e.g., [26–30]). Hence, in this work, the geochemistry and mineralogy of two Ni-laterite profiles of the San Felipe deposit has been revisited, making special emphasis on the abundance, textures, and mineral chemistry of Ni-bearing phyllosilicates.

2. Geological Setting

The San Felipe deposit is located on the San Felipe plateau (in Spanish, *Meseta de San Felipe*), an erosional remnant near Camagüey city, with a total extension of 50 km^2, a slight inclination from SSE to NNW, and with elevations between 140 and 190 masl. The San Felipe deposit is located at the north of the province of Camagüey, 30 km to the NW of the city of Camagüey, and 70 km SW of the city of Nuevitas (Figure 1a and 1b; [26–30]. The current nickel resource of San Felipe deposit is 250 Mt at 1.43 % Ni and 0.05 % Co [25].

The San Felipe weathering profile is developed on the serpentinized peridotite of the Camagüey ophiolitic massif (COM). This massif is part of the so-called Northern Cuban Ophiolitic Belt [31], and has been dated as early Cretaceous [32]. These ultramafic bodies represent slices of oceanic lithosphere obducted onto the North American continental margin in the Latest Cretaceous to Late Eocene time during the collision between the volcanic arc of the Caribbean with Jurassic-Cretaceous passive margins (Figure 1c; [31,33].

Camagüey peridotites are essentially made up of mantle tectonites with subordinate gabbro sills and dykes. Mantle peridotites mainly consist of clinopyroxene-rich harzburgite, harzburgite, and minor dunite. Uplift exposed the peridotite bodies to laterization in the beginning of the Miocene [34].

In the field, the material outcropping at the top of the San Felipe plateau displays dark red and yellowish ochre colors (Figure 2a), with discrete centimeter to meter-sized ferricrete and silica blocks. In general, the weathering profile in San Felipe includes the following, from the bottom to the top: (i) ophiolitic peridotite parent rock; (ii) saprolite; (iii) clay zone (smectite > serpentine); iv) ferruginous clay-zone (Fe oxyhydroxides > smectite) ; (v) oxide zone (Figure 2b); and v) ferricrete (Figure 2c and d) with free silica concretions [29]. The latter is an essential feature of San Felipe laterite profile (Figure 2e, f).

Preprints (www.preprints.org) | NOT PEER-REVIEWED | Posted: 4 August 2023 doi:10.20944/preprints202308.0428.v1

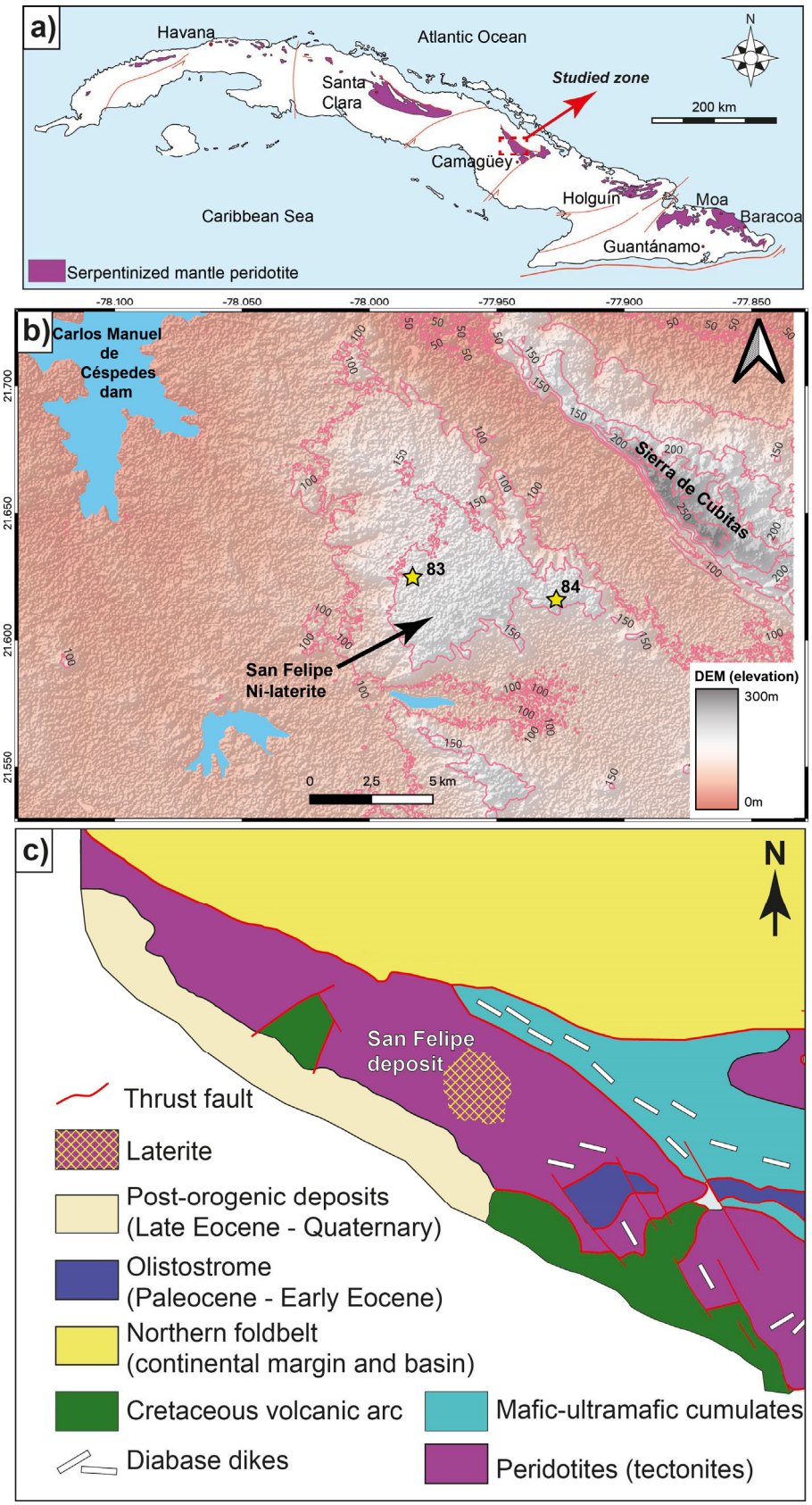

Figure 1. a) Location of the Camagüey ophiolite Massif in central Cuba. b) Geographic location of the San Felipe Ni-Co deposit in Camagüey Province, Cuba. Hillshaded DEM is based on SRTM 30 m model [35]. Contour lines represent elevations with 50 m interval. Physiographic features are based on naturalearthdata.com database [36]. Coordinate Reference System: EPSG:4326-WGS 84. c) Simplified geological map of the study area indicating the San Felipe deposit [30].

Preprints (www.preprints.org) | NOT PEER-REVIEWED | Posted: 4 August 2023 doi:10.20944/preprints202308.0428.v1

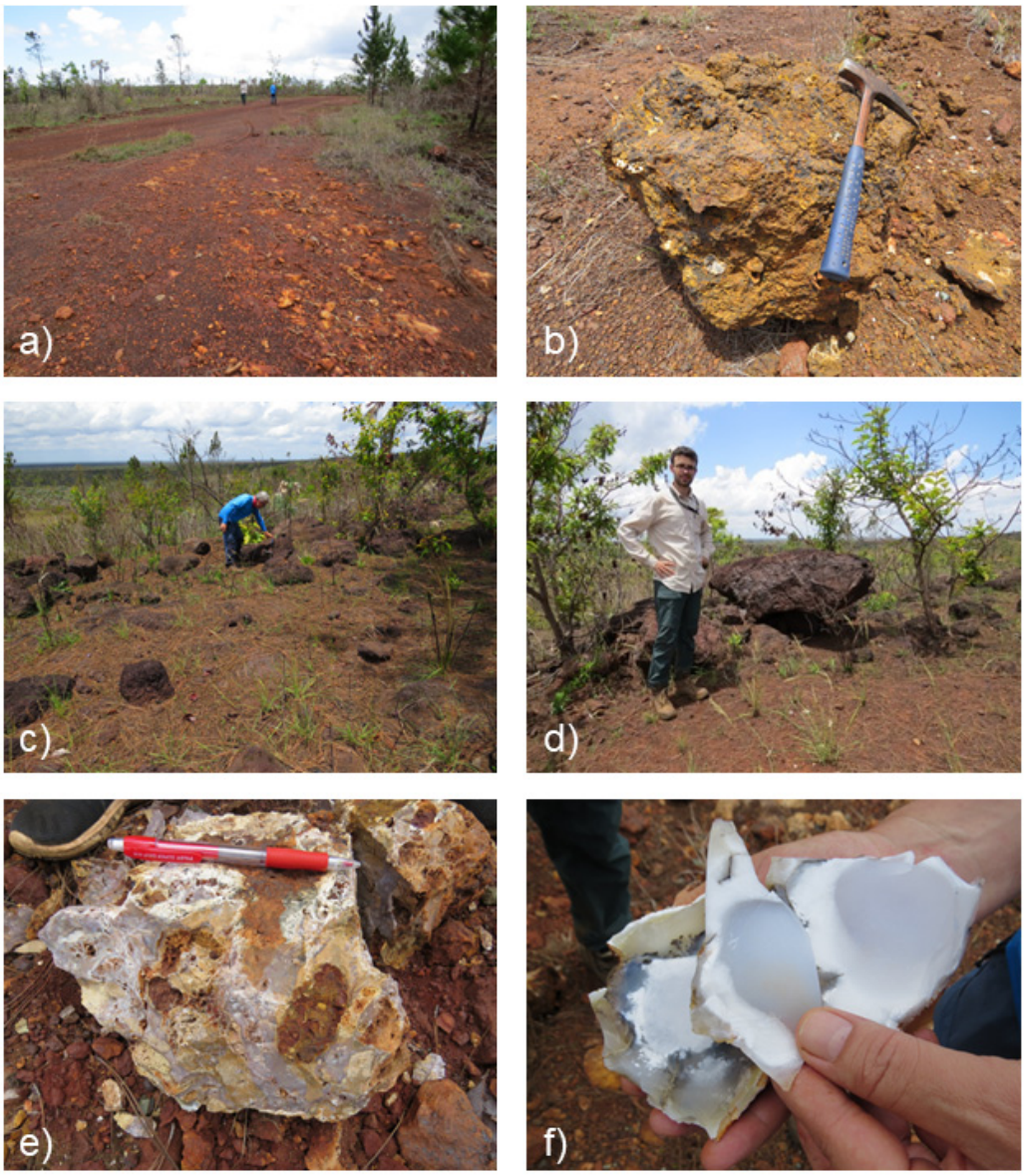

Figure 2. Images of San Felipe Ni-laterite outcrops. a) General view at the top of the plateau, the material outcropping is of dark red color, and is characterized by sparse, low vegetation. b) Ochre to dark brown goethite and hematite concretion laying on top of the oxide zone. c-d) Centimeter to meter-sized ferricrete blocks. e) Amorphous silica or microcrystalline quartz decimeter-sized nodules, their internal translucent to opaque white appearance is shown in (f).

3. Materials and Methods

3.1. Sampling

The studied samples were collected from two representative cores (named 83 and 84) of the San Felipe deposit (Figure 1b), where a previous prospection was carried out by the Asociación Económica Internacional Geominera S.A. and San Felipe Mining Ltd., in grids ranging from 1000x1000 m to 12.5x12.5 m in areas of special interest (Figures 1b, c). Since cores 83 and 84 represent a continuous sampling of the corresponding laterite profiles, they are going to be referred to as cores and profiles in this work equally. Core 83 was drilled in the central part of the plateau and is 24 m in length, and can be divided into three horizons, from top to bottom [37]: i) reddish oxide zone (1 m thick); ii) reddish brown ferruginous saprolite (14 m); and iii) dark, greenish brown saprolite (9 m). Core 84 was drilled at the border of the plateau and is 12 m in length, and consists of four horizons: i) oxide zone (1 m); ii) ferruginous saprolite (1 m); iii) saprolite (8 m); and iv) green, slightly weathered

Preprints (www.preprints.org) | NOT PEER-REVIEWED | Posted: 4 August 2023 doi:10.20944/preprints202308.0428.v1

peridotite (2 m). The bedrock consists of a serpentinized clinopyroxene-rich peridotite, locally intruded by gabbros, but it was not sampled in neither of the cores. A total number of 21 samples were selected, 9 of which belong to core 83, and 12 to core 84. The textural characteristics of the hand samples in the main horizons are illustrated in Figure 3. Samples from higher levels are more porous and crumblier, and contain goethicized nodules (Figure 3a, 3b). Downward in the profile, samples become more compact, and fractures with a green infilling are observed (Figures 3b, 3c). The ferruginous saprolite in profile 83 (Figure 3d) presents fragments of cryptocrystalline quartz aggregates. In core 84, samples from the saprolite at a depth of 7 m display fractured and porous fragments of the parent rock, surrounded and filled by brown-black Fe oxyhydroxide grains (Figure 3e). At the bottom, the slight weathering on serpentinised peridotite (sample 84-12) provides a dark green to the rock (Figure 3f).

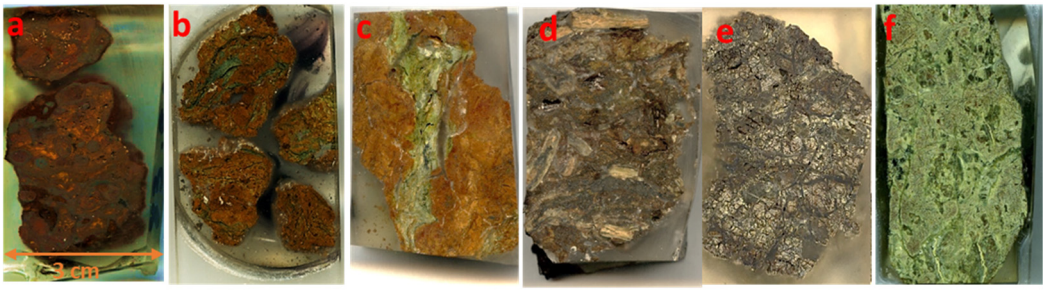

Figure 3. Images of hand specimens embedded in epoxy resin of the two studied cores: a) sample 83-01 from the oxide zone; b) sample 83-04 from the ferruginous saprolite; c) sample 83-10 from the ferruginous saprolite, including green infillings in fractures; d) sample 83-15 with cryptocrystalline quartz, from the ferruginous saprolite; e) sample 84-07 from the saprolite; f) sample 84-12 from the slightly weathered serpentinized peridotite. The scale for the six images is the same as in a). The sample names are composed of the code of the core (83- or 84-) and a number that indicates the depth of the sample (e.g., "83-01" refers to the sample collected at 1 m from core 83).

3.2. Analytical methods

Bulk-rock geochemical analyses were performed at the Centro de Instrumentación Científica of the Universidad de Granada (CIC-UGR, Granada, Spain). Major element concentrations were obtained by X-ray Fluorescence (XRF) spectrometry on glass beads using a Philips PV1404 spectrometer. Precision was better than ±1.5% for a concentration of 10 wt.%. The analyses were recalculated to an anhydrous 100 wt.% basis. Further details on the analytical technique can be found in [38].

Random powder X-ray diffraction (XRPD) and oriented aggregate mount X-ray diffraction (XRD, (air dry, ethylene glycol and heated to 550°C) analyses were obtained at Centres Científics i Tecnològics of the Universitat de Barcelona (CCiT-UB, Barcelona, Spain), in a PANalytical X'Pert PRO MPD Alpha1 powder diffractometer in Bragg–Brentano θ/2θ geometry of 240 mm of radius, nickel filtered Cu Kα1 radiation (λ = 1.5406 Å), 45 kV and 40 mA. The samples were scanned from 4 to 100° (2θ) with a step size of 0.017° and measuring time of 150 s per step, using an X'Celerator detector (active length = 2.122°). Mineral identification was facilitated by X'Pert Highscore search-match software using the powder diffraction database of the International Centre for Diffraction Data (ICDD). For the estimation of the relative amounts between identified mineral phases, the quantitative Rietveld analysis method [39] with the software Topas V4.2 [40] was used.

The selected samples were embedded in epoxy resin and prepared as thin sections, polished using non-aqueous fluids to prevent damage on mineral phases. The mineralogy and microtextural features of the thin sections were first examined with a Nikon Eclipse LV100 POL optical microscope (OM). The sections were later carbon coated and studied with an environmental scanning electron microscope (ESEM) Quanta 200 FEI, XTE 325/D8395, coupled with an energy dispersive X-ray

Preprints (www.preprints.org) | NOT PEER-REVIEWED | Posted: 4 August 2023 doi:10.20944/preprints202308.0428.v1

spectrometer (EDS), and a JEOL JSM-7001F field emission SEM (FE-SEM), both equipped with secondary (SE) and backscattered electron (BSE) detectors, under 20 kV, at the CCiT-UB.

Quantitative electron microprobe analyses (EMPA) were also conducted on the carbon coated polished thin sections at the CCiT-UB using a five-channel JEOL JXA-8230 operating in wavelength dispersive spectroscopy (WDS) mode. The analytical conditions were 15-20 kV accelerating voltage, 10-20 nA beam current, 1-2 μm beam diameter, and 10-20 s counting time per element; and the XPP matrix correction was used [41]. The measurements and the calibrations were made using the following natural and synthetic standards: diopside (Si; TAP), Al_2O_3 (Al; TAP), wollastonite (Ca; PET), orthoclase (K; PET), periclase (Mg; TAP), albite (Na; TAP), Fe_2O_3 (Fe; LIF), CoO (Co; LIF), NiO (Ni; LIF), rhodonite (Mn; LIF), Cr_2O_3 (Cr; LIF), V (V; LIF), and rutile (Ti; LIF). Iron in the weathered minerals was assumed to be Fe^{3+} (e.g., [9,42–44]).

4. Results

4.1. Major elements geochemistry

Major elements composition of both profiles and loss on ignition (LOI) data are given in Supplementary Material Table S1 and in Figures 4a and 4b, as a function of depth.

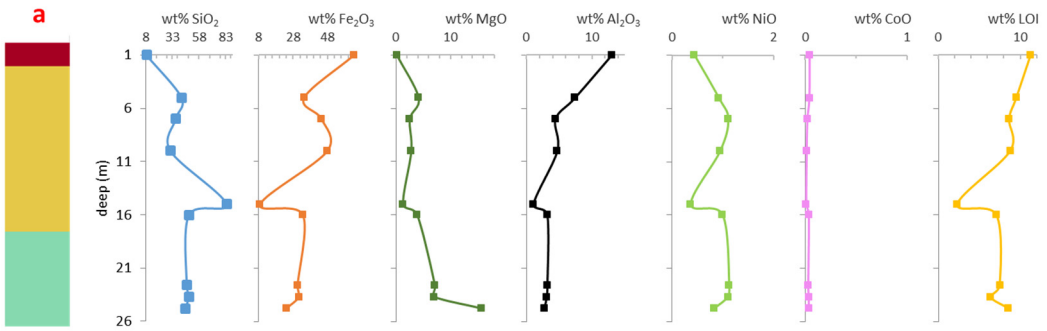

Figure 4. Simplified laterite profiles of the studied cores of San Felipe (red: oxide zone; yellow: ferruginous saprolite; light green: saprolite; olive green: weathered peridotite), and geochemical composition in wt.% of the bulk samples with depth: a) core 83, b) core 84.

The composition in terms of SiO_2 and Al_2O_3 is similar in both profiles, with a decrease of SiO_2 and MgO, and an increase of Al_2O_3 and Fe_2O_3 to the top. The SiO_2 content in profile 83 is 45.4 wt.% at the base and 8.8 wt.% at the oxide horizon, with an anomalous abrupt increase to 84.2 wt.% at 15 m depth that is not observed in profile 84, where SiO_2 ranges from 44.5 to 32.2 wt.%. Aluminum ranges from 2.7 at the saprolite horizon to 13.0 wt.% Al_2O_3 in profile 83, and 1.2 to 7.7 wt.% in profile 84. Iron is more abundant in profile 83, and varies from 33.6 wt.% to 63.3 wt.% Fe_2O_3, with three maxima at the oxide zone, the ferruginous saprolite and the saprolite, and an abrupt decrease at 15 m depth (8.9 wt.%). The curves for SiO_2 and Fe_2O_3 in profile 83 are almost symmetrical, indicating a strong negative correlation between them. In profile 84, Fe_2O_3 increases continuously between 11.9 wt.% and 32 wt% from the base to the top. Magnesium is more abundant in profile 84, from 29.9 wt.% MgO at the base to 4.8 wt.% at the top, and from 15.7 to 0.2 wt.% in profile 83. In core 84 there is an important increase of NiO at 6 m deep (3.6 wt.%). Nickel varies from 0.33 wt.% to 0.91 wt.% in profile 84 and from 0.44 wt.% to 0.83 wt.% in 83. Cobalt is below than 0.05 wt.% CoO in core 83, and up to 0.18 wt.% CoO in core 84. The LOI presents an opposite behavior in each core, increasing towards the top in profile 83 (8.6 to 11.3 wt.%) with an abrupt decrease at 15 m (2.3 wt.%), and decreasing towards the top in profile 84 (10 to 5.2 wt.%).

4.2. Petrography

The base of core 84 is formed by a slightly weathered, serpentinized peridotite that does not preserve most of the primary mantle mineralogy. Despite that under the OM some of the primary

Preprints (www.preprints.org) | NOT PEER-REVIEWED | Posted: 4 August 2023 doi:10.20944/preprints202308.0428.v1

textures can be observed, olivine and pyroxene have been almost completely substituted by phyllosilicates and Fe oxides during serpentinization (Figure 5). Euhedral to subhedral sections of pyroxene grains of 1 mm in length have been altered to serpentine group minerals (lizardite and chrysotile) along cleavage planes, with thin, brown goethite discontinuous intergrowths (Figure 5a). There are fractures crosscutting the grains replaced by serpentine (Figure 5a, 5b). Pseudomorphs or voids left by olivine grains of about 0.2 mm in diameter are surrounded by minerals of the serpentine group (lizardite and chrysotile) and Fe oxide (magnetite/maghemite) small grains. Serpentine is regularly associated with micrometric-sized grains of magnetite distributed along fractures (Figure 5c). Cores of olivine grains are replaced by microcrystalline aggregates of needle- or platelet-shaped smectite (hereafter incipient smectite), which exhibit 2nd order interference colors (Figures 5c, 5d).

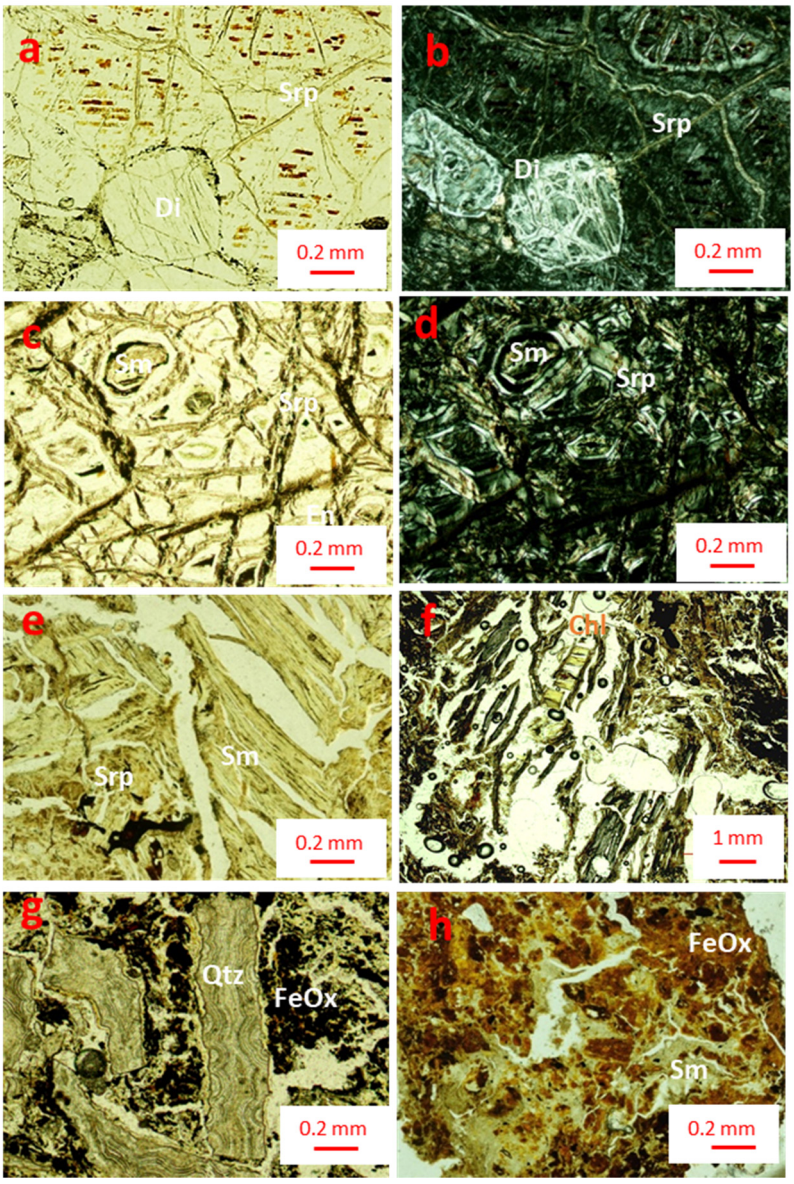

Figure 5. Optical photomicrographs taken with plane polarized light (a,c,e,g,h) and crossed polars (b,d,f) of the characteristic textures of the main mineralogy in the San Felipe Ni-laterites: a-b) pyroxene grains with green serpentine in fractures, and red-brown goethite films (sample 84-12, weathered peridotite); c-d) olivine grain with green serpentine in fractures and black magnetite/maghemite, the nucleus of a greenish olivine grain can be observed, containing incipient smectite (sample 84-12, weathered peridotite); e) fractured green serpentine grains of more than 1 mm long partially substituted by type I smectite (sample 84-08, saprolite); f) chlorite as vein bridging between smectite grains; g) angular fragments of botryoidal cryptocrystalline quartz aggregates surrounded by iron oxyhydroxides (sample 83-15, ferruginous saprolite); h) irregular green aggregates of smectite type

 doi:10.20944/preprints202308.0428.v1

II, some of them dyed by iron oxyhydroxides (sample 83-04, ferruginous saprolite). Key: En = enstatite; Srp = serpentine; Sm = smectite; Chl= chlorite; Qtz = quartz; FeOx = Fe oxyhydroxides.

The original texture of the bedrock in the intermediate saprolite and the ferruginous saprolite is lost in both profiles (from 23 to 1 m depth in core 83, and from 9 to 1 m in core 84). This part of the profile is more porous and presents foliated and bent, green smectite crystals of more than 1 mm in length, that leave elongated voids due to their cleavage. These crystals are the result of an almost complete substitution of the primary minerals, mainly pyroxene, by a secondary mineral of the smectite group (hereafter type I smectite), and in some areas by irregular phyllosilicate grains that appear dark red due to the presence of iron oxyhydroxides (sample 84-08, Figure 5e). Chlorite appears as- a vein bridging between smectite grains (Figure, 5f). Some samples of intermediate saprolite in profile 83 (15 m) have a slightly different mineralogy, with irregular brown accumulations of Fe oxyhydroxides and slightly deformed angular fragments of botryoidal silica aggregates, of approximately 2 x 0.2 mm (Figure 5g). This texture may suggest that these fragments come from a silicified vein that collapsed. In the ferruginous saprolite, irregular green deformed grains of phyllosilicates (lizardite and type II smectite) up to 0.2 mm in length are surrounded by irregular brown Fe oxyhydroxide aggregates (sample 83-4, Figure 5h).

SEM images of a weathered peridotite sample reveal the texture of fractured, pseudomorphed olivine grains of about 1 mm in size wrapped by layers of serpentine and smectite or kerolite-type minerals with different average Z values (Figure 6a). Dissolution voids in the olivine cores are partially filled by disordered aggregates of incipient smectite platelets and Fe oxides (magnetite/maghemite) (Figure 6b). Original orthopyroxenes hosting clinopyroxene exsolution lamellae evolve to smectite at different rates, being the clinopyroxene exsolutions more quickly substituted (to incipient smectite) (Figure 6c). In addition, abundant Cr-spinel grains are present associated with pyroxene, and may occur as euhedral octahedral crystals, anhedral crystals or as inclusions in former pyroxene (Figure 6d). In the saprolite of core 84, needles and platelets of type I smectite have been observed (Figure 6e). In the porous ferruginous saprolite, bent tabular grains of serpentine (lizardite) contain cores of type II smectite (Figure 6f). Iron oxides occur as inclusions in serpentine or within fractures crosscutting serpentine in sample 83-22 (Figure 6g). Cr-spinel can also be found as fractured, isolated and euhedral crystals, substituted by Fe oxides (Figure 6h).

Preprints (www.preprints.org) | NOT PEER-REVIEWED | Posted: 4 August 2023 doi:10.20944/preprints202308.0428.v1

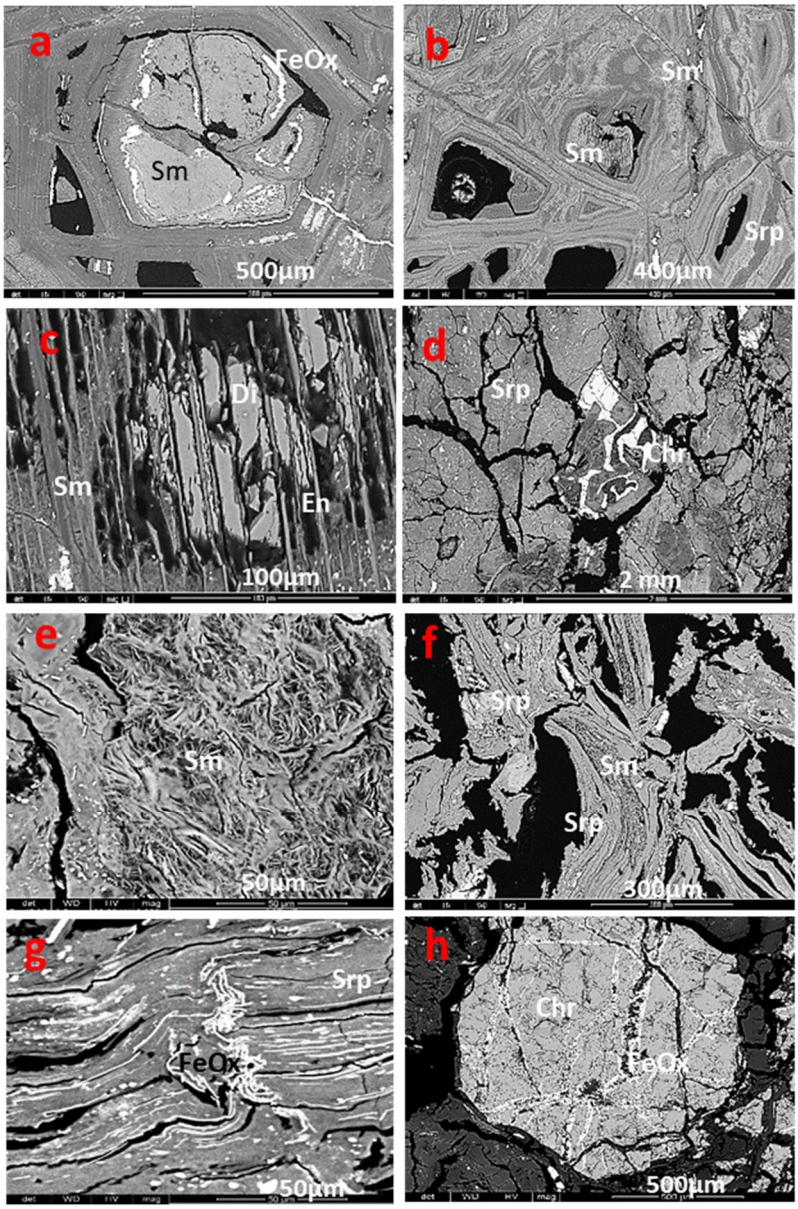

Figure 6. BSE photomicrographs of the textures observed in the San Felipe Ni-laterite: a) olivine grain altered to incipient smectite surrounded by magnetite/maghemite (sample 84-12, weathered peridotite); b) different generations of serpentine and smectite (sample 84-12, weathered peridotite); c) orthopyroxene grain with exsolutions of clinopyroxene, altered to incipient smectite (sample 84-12, weathered peridotite); d) Cr-spinel as intra/inter crystals associated with pyroxene surrounded by serpentine (sample 84-09, transition between weathered peridotite and saprolite); e) randomly oriented needles and platelets of type I smectite, (sample 84-09, transition between weathered peridotite and saprolite); f) deformed platy serpentine crystals altered to type II smectite at the nuclei, and inclusions of Fe oxyhydroxides (sample 84-02, ferruginous saprolite); g) serpentine with Fe oxyhydroxides in fractures and as inclusions (sample 83-15, ferruginous saprolite); h) euhedral Cr-spinel crystal with Fe oxides within fractures (sample 84-09, transition between weathered peridotite and saprolite horizon). Key: En = enstatite; Di = diopside; Srp = serpentine; Sm = smectite; Qtz = quartz; FeOx = oxides/oxyhydroxides; Chr = Cr-spinel.

4.3. Mineral chemistry

Our results show that type I smectites (found in the saprolite of core 84, Figure 5e) and type II smectites (in both cores 83 and 84, Figure 5f) display distinct compositions (Supplementary Material Table S2, Figure 7).

Preprints (www.preprints.org) | NOT PEER-REVIEWED | Posted: 4 August 2023 doi:10.20944/preprints202308.0428.v1

The average chemical composition of type I smectite in sample 84-09 (Figure 6), in the transition between the weathered peridotite and the saprolite horizon, is 43.52 wt.% SiO_2, 2.04 wt.% Al_2O_3, 14.83 wt.% MgO, 15.46 wt.% Fe_2O_3 and 2.58 wt.% NiO, and the corresponding structural formula is: $(Mg_{1.90}Fe_{0.90}Ni_{0.19})_{\Sigma=2.99}(Si_{3.64}Al_{0.15})O_{10}(OH)_2Ca_{0.03}Na_{0.02}$. In core 84, type II smectite in the serpentine tabular grains, in the ferruginous saprolite (sample 84-02), has an average chemical composition of 46.53 wt.% SiO_2, 2.92 wt.% Al_2O_3, 3.62 wt.% MgO, 20.58 wt.% Fe_2O_3 and 2.76 wt.% NiO. The corresponding structural formula is $(Fe_{1.33}Mg_{0.51}Al_{0.21}Ni_{0.10})_{\Sigma=2.15}(Si_{3.93}Al_{0.07})O_{10}(OH)_2Ca_{0.03}Na_{0.03}$. Type II smectite from core 83 has an average of 43.06 wt.% SiO_2, 2.38 wt.% Al_2O_3, 4.57 wt.% MgO, 22.29 wt.% Fe_2O_3 and 1.06 wt.% NiO (Figure 7c), and a structural formula of $(Fe_{1.44}Mg_{0.57}Ni_{0.07})_{\Sigma=2.08}(Si_{3.82}Al_{0.18})O_{10}(OH)_2Ca_{0.02}Na_{0.03}$. The interlaminar cations are Ca and Na in both types and the occupancy is < 0.06, far from the usual values of hydrated exchangeable cations (x ≈ 0.2-0.6) in smectites [45]. This contrasts with the incipient smectite from the slightly weathered, serpentinized peridotite in core 84, which has an average structural formula of $Mg_{2.46}Fe_{0.38}Ni_{0.02}Si_{3.69}Al_{0.09}O_{10}(OH)Ca_{0.02}Na_{0.01}$ [37], and formed as a substitution of olivine and pyroxene.

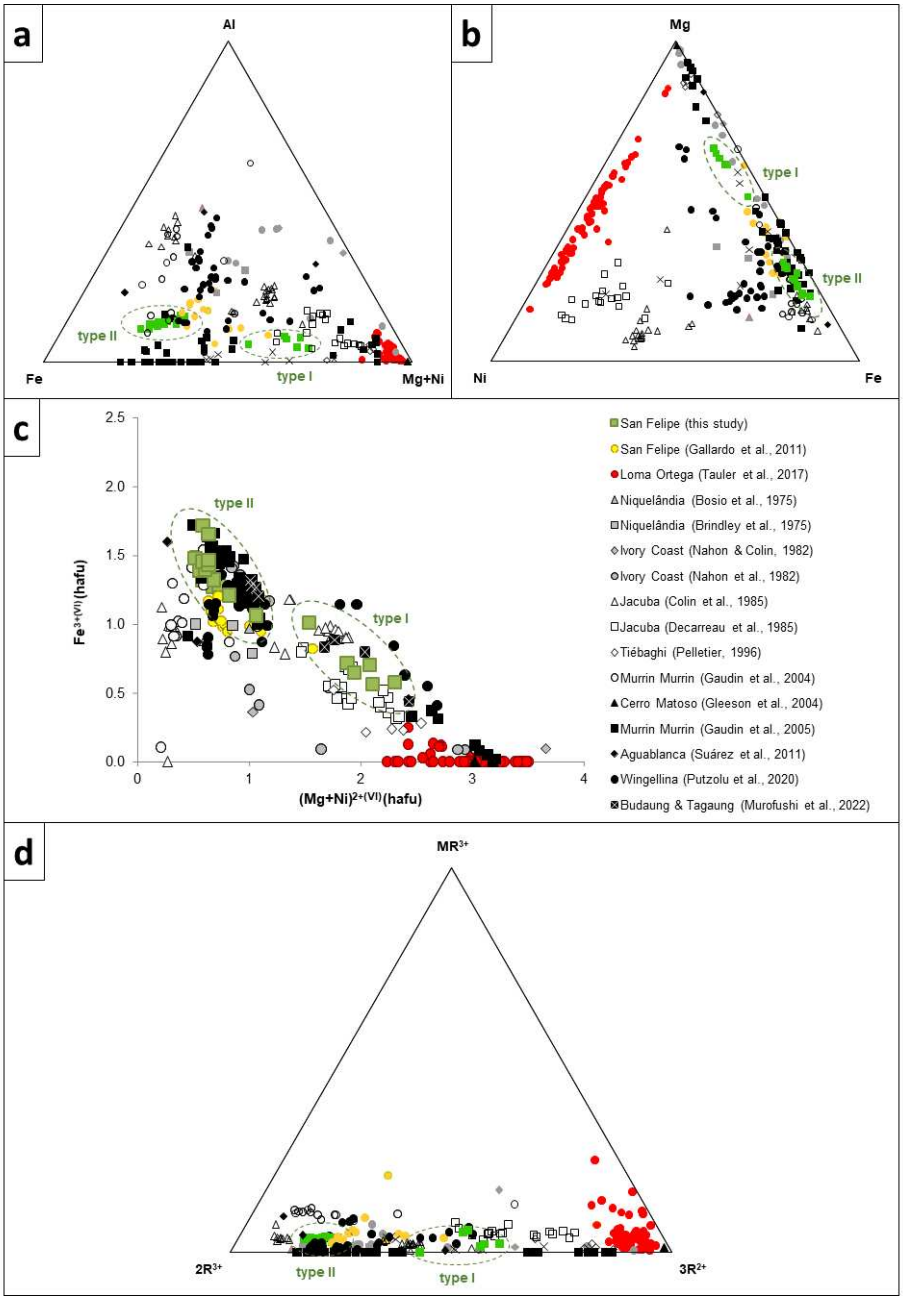

Preprints (www.preprints.org) | NOT PEER-REVIEWED | Posted: 4 August 2023 doi:10.20944/preprints202308.0428.v1

Figure 7. Mineral chemistry of Ni-smectite from San Felipe (this study and from TEM data from [37], compared with Ni-Fe-Mg smectites worldwide, including Loma Ortega (Dominican Republic, [24]), Niquelândia Brazil [46,47], Ivory Coast [48,49], Jacuba, Brazil [22,42], Tiébaghi, New Caledonia, [50], Murrin Murrin, Australia, [9,51], Cerro Matoso, Colombia, [52], Aguablanca, Spain,[53], Wingellina, Australia, [23], Budaung and Tagaung, Nyamar [54]. a) Fe^{3+}-Al-(Mg + Ni) ternary plot (based on [22]); b) Ni-Mg-Fe^{3+} ternary plot; c) octahedral Fe^{3+} versus (Mg + Ni) binary diagram representing the octahedral cations in smectite (modified from [22]; and d) MR^{3+}-$2R^{3+}$-$3R^{2+}$- (based on [55], in which MR^{3+} = Na + K + (Ca/2), $2R^{3+}$ = Al + Fe^{3+} - MR^{3+}, and $3R^{2+}$ = Mg + Ni + Mn. Data has been plotted as hafu (calculated on the basis of 11 oxygens), and all Fe has been considered trivalent.

Serpentine in San Felipe can be divided, according to their Ni content, into low-Ni (so-called serpentine I) and Ni-enriched (serpentine II). The average composition of serpentine II grains in sample 84-7 (Figure 8d and Supplementary Material Table S3) is 39.92 wt.% SiO_2, 2.05 wt.% Al_2O_3, 25.33 wt.% MgO, 7.75 wt.% Fe_2O_3 and 3.23 wt.% NiO. The corresponding structural formula is $(Mg_{1.97}Fe_{0.30}Ni_{0.14}Al_{0.13})Si_{2.09}O_5(OH)_4$ (Supplementary Material Table S3, Figure 9).

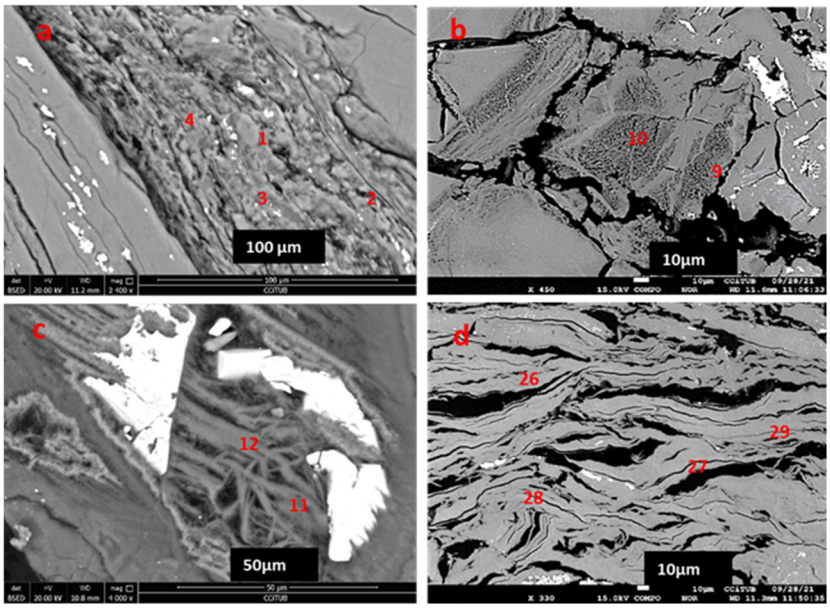

Figure 8. BSE photomicrographs of smectite textures and serpentine in San Felipe and points of the analysis presented in Table S3: a) Type II smectite (sample 84-02); b) Type I smectite after olivine (sample 84-09); c) type I smectite after pyroxene (sample 84-09); d) serpentine in the saprolite (sample 84-07). The point analyses 84-02-1, 2, 3 and 4 correspond to smectite type II; point analyses 84-09-9 and 84-09-10 are smectite after olivine; and analyses 84-09-11 and 84-09-12 are smectite after pyroxene.

Preprints (www.preprints.org) | NOT PEER-REVIEWED | Posted: 4 August 2023 doi:10.20944/preprints202308.0428.v1

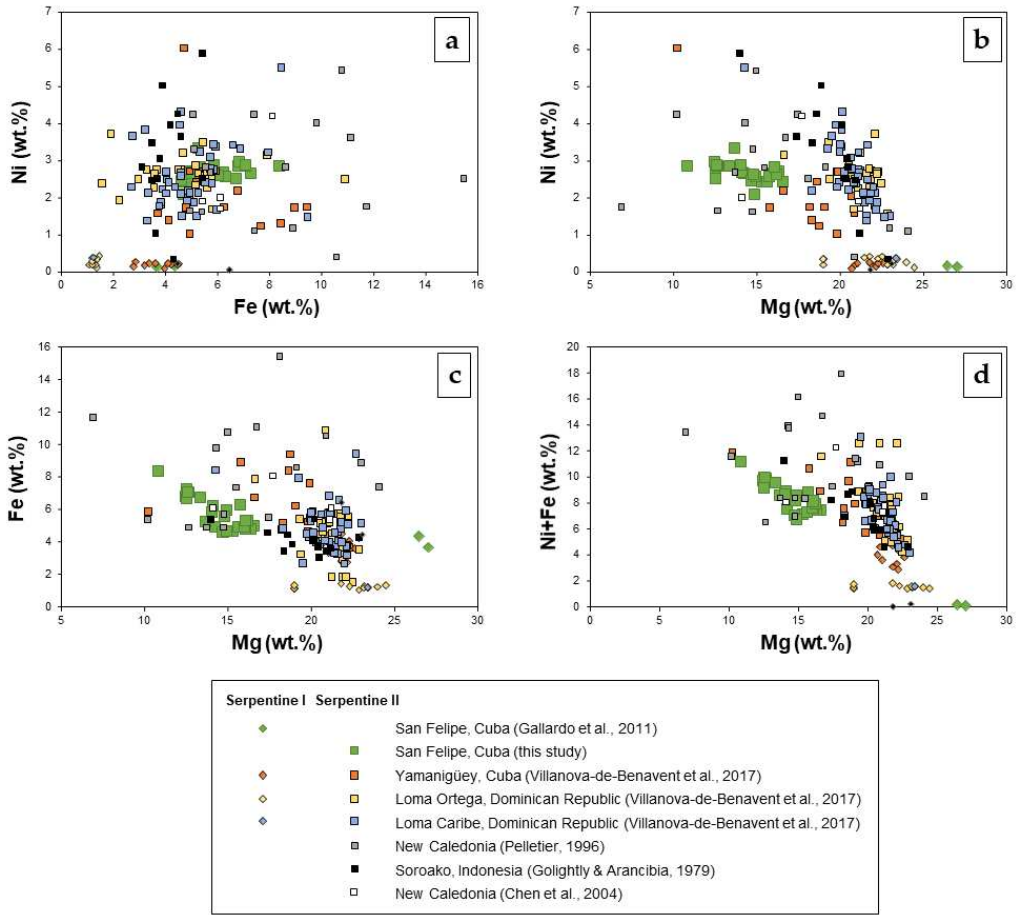

Figure 9. Composition of serpentine I and II (this study) from San Felipe compared to serpentine I and II from other localities: Yamanigüey (Cuba), Loma Ortega and Loma Caribe (Dominican Republic) [44], New Caledonia [50,56] and Soroako, Indonesia [57], in terms of the major octahedral elements (Mg, Fe, Ni in wt.%). a) Ni versus Fe (wt.%), b) Ni versus Mg (wt.%), c) Fe versus Mg (wt.%), and d) Ni+Fe versus Mg (wt.%).

The EMPA mapping of Si, Mg, Fe, Ni and Al of a representative completely pseudomorphed olivine grain (Figure 10) gives compositions that are consistent, in the core, with a trioctahedral smectite type I rich in Fe and with a Ni content of around 3 wt.% (Supplementary Material Table S2), crosscut and surrounded by a Ni- and Fe-enriched serpentine.

Preprints (www.preprints.org) | NOT PEER-REVIEWED | Posted: 4 August 2023 doi:10.20944/preprints202308.0428.v1

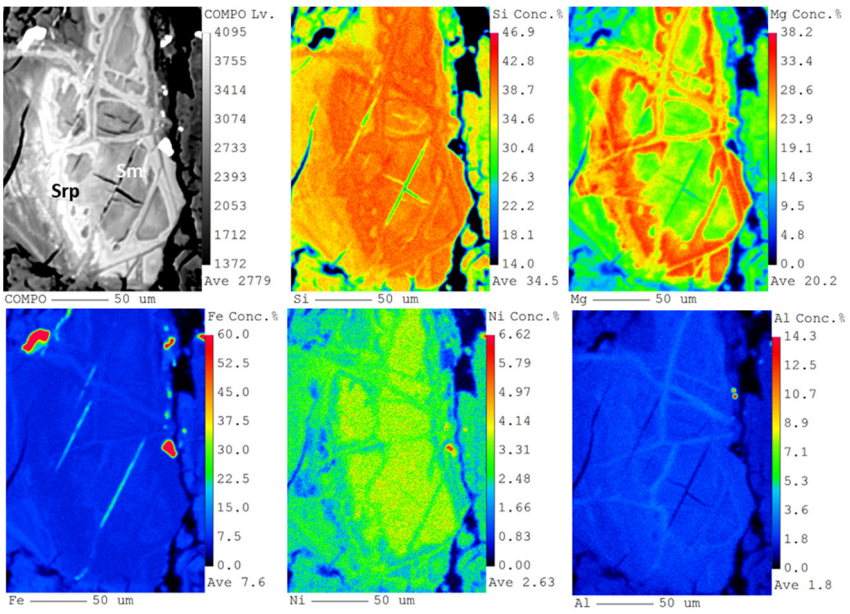

Figure 10. BSE photomicrograph (top left) and Si, Mg, Fe, Ni and Al X-ray elemental maps obtained by EMPA of a type I smectite grain from sample 84-09 (transition between the serpentinized peridotite and the saprolite).

4.4. Structure characterization of minerals by X-ray diffraction (XRD)

The mineral phases identified in cores 83 and 84 and their relative amounts as a function of depth are given in Supplementary Material Table S4 and Figure 11 displays the XRPD of selected samples. The minerals identified are smectite, dehydrated or collapsed smectite (with a talc-like or kerolite-like structure), serpentine (lizardite and chrysotile), chlorite, quartz, hematite, goethite, maghemite and Cr-spinel. As discussed later, quantification of nanometric-sized, hydrated phyllosilicates and in particular smectite and kerolite-like structures by Rietveld profile analysis is problematic [58–60]. In sample 83-25, smectite presents an intense, broad, symmetric peak at 14.7 Å, and a kerolite faint wide reflection at 9.6 Å (Figure 8). However, at higher angles, both phases present almost coincident broad asymmetric *hk* diffraction bands which are a typical feature of turbostratic structures [61]. Accordingly, smectite and kerolite have been quantified together due to the similarity of their XRPD patterns. Whenever the smectite broad 14.7 Å peak is important, we will refer to possible mixtures of smectite/kerolite as "smectite".

In order to get further evidence on the presence of smectite, XRD of oriented aggregate mounts have been obtained for a sample of core 83 (83-7) and another of core 84 (84-12) (Figures 11a* and 11c*, respectively). In sample 83-7, the symmetrical peak at d_{001}=14.7 Å corresponds to a pure smectite having two water layers [62,63]. After heating at 540°C, the d_{001} collapses to 9.9 Å. With ethylene glycol (EG), d_{001}=14.7 expands to 17.3 Å as symmetrical peaks, indicating a uniform swelling of almost all the layers without mixing with the non-swelling talc/kerolite layers [58] (Figure 11b). In sample 84-12, after heating at 540 °C, the d_{001} collapses to 9.6 Å. With EG, d_{001}=14.3 expands to 17.0 Å as a symmetrical peak (Figure 12).

In profile 83, smectite decreases from the base to the top (83.3 and 24.3 wt.%, respectively), and so does chlorite (4.3 at the base to 3.0 wt.% near the top). In contrast, lizardite decreases (0.3 wt.% at 25 m and 0.6 wt.% at 1 m). Profile 84 is dominated by smectite (74.0 to 17.3 wt.%) and serpentine (lizardite plus chrysotile) (24.6 wt.% at the bottom to 2.3 wt.% at the top). Near the middle of profile 83 (at 16 m depth), a highly silicified level appears, with more than 50 wt.% quartz. In core 84, quartz is less important, only 18.2 wt.% at the top. Magnetite/maghemite decrease from the base to the top, whereas goethite and hematite increase towards the top. Near the surface, the total amount of goethite and hematite is similar in both profiles (69.3 and 60.3 wt.%), but the percentage of goethite in core 83 doubles that of core 84. In Figure 12, the variation of the major mineral phases is represented as a function of depth. It is worth noting that smectite is always dominant along both profiles

Preprints (www.preprints.org) | NOT PEER-REVIEWED | Posted: 4 August 2023 doi:10.20944/preprints202308.0428.v1

(Supplementary Material Table S4), hence the horizons that have been labeled in section 3.1 as saprolite and ferruginous saprolite, should be defined as clay-rich saprolite and ferruginous clay-rich saprolite, instead.

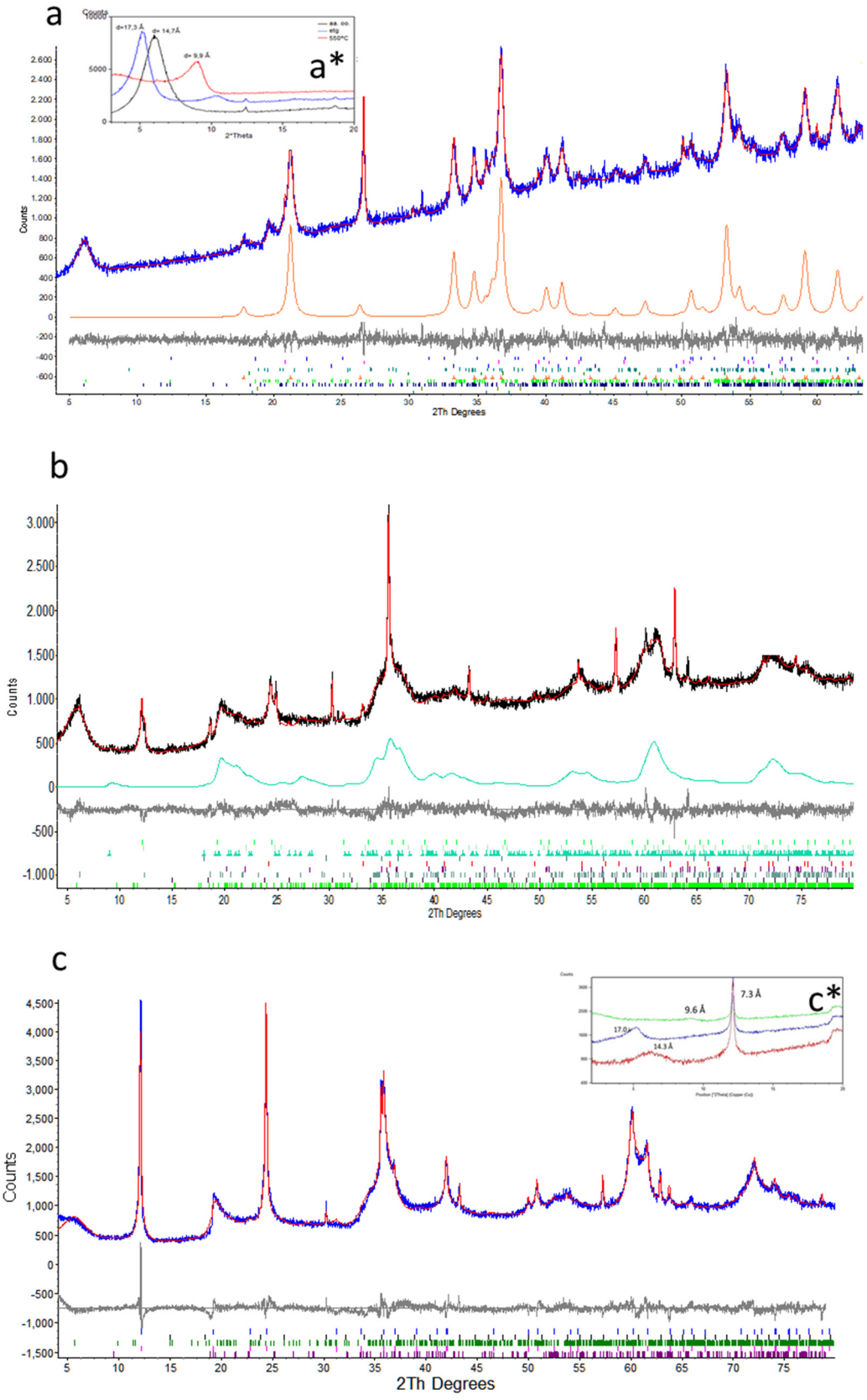

Preprints (www.preprints.org) | NOT PEER-REVIEWED | Posted: 4 August 2023 doi:10.20944/preprints202308.0428.v1

Figure 11. a) XRPD refinement of sample 83-7 (ferruginous saprolite horizon), Rwp (numerical figure of merit quantifying the quality of the fit) = 3.3. Legend: blue = experimental pattern, red= calculated pattern, black = difference between experimental and calculated pattern, orange = calculated pattern for goethite. At the bottom, the Bragg reflections for each mineral phase; a*) XRD of oriented aggregate mounts of the same sample since 2θ degrees. Legend: black = untreated sample at room temperature, blue = treated with ETG, reed = heated to 540°C; b) XRPD refinement of sample 83-25 (saprolite horizon), Rwp = 4.5. Legend: black = experimental pattern, red = calculated pattern, grey = difference between the experimental and the calculated pattern, green = calculated pattern for a talc-like structure (kerolite). At the bottom, the Bragg reflections for each mineral phase are shown; b) XRPD refinement of sample 83-7 (ferruginous saprolite horizon), Rwp = 3.3. Legend: blue = experimental pattern, red= calculated pattern, black = difference between experimental and calculated pattern, orange = calculated pattern for goethite. At the bottom, the Bragg reflections for each mineral phase. c) XRPD refinement of sample 84-12 (weathered peridotite), Rwp = 6.9, legend as a); c*) XRD of oriented aggregate mounts of sample 84-12. Legend: reed = untreated sample at room temperature, blue = treated with ETG, green = heated to 540°C.

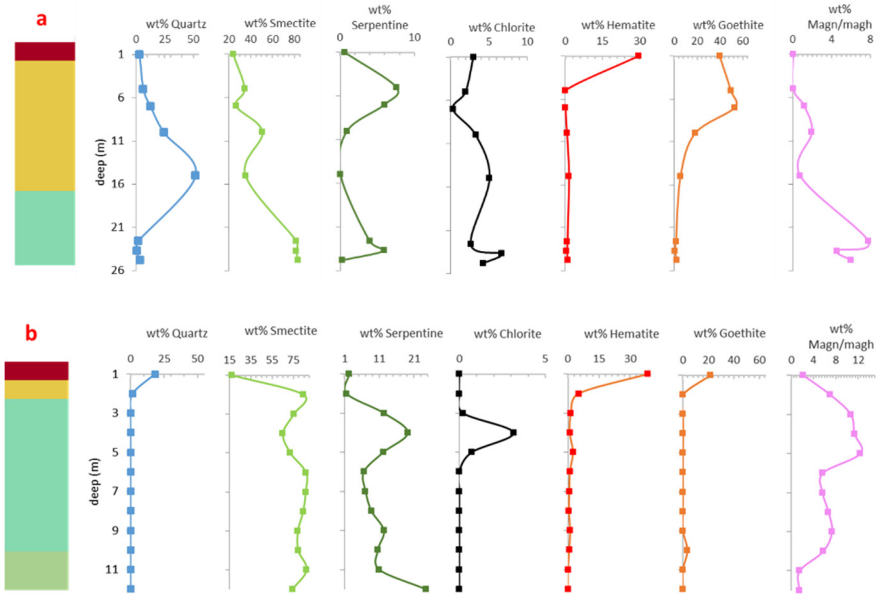

Figure 12. Variation in wt.% of mineral phases in function of depth: a) core 83; b) core 84.

5. Discussion

5.1. Degree of weathering

The geochemical analyses (Figure 3) agree with the XRPD mineralogical composition (Supplementary Material Table S4, Figure 10). The SiO_2 wt.% decreases in the two profiles in the ferruginous saprolite but in profile 83 there is an abrupt increase at 15 m deep that corresponds to the occurrence of cryptocrystalline quartz millimetric to centimetric fragments (Figure 5g). This interruption in the typical regular succession of horizons explains the observed differences between profiles 83 and 84 at this depth. The increase of silica is accompanied by a reduction of Al_2O_3, Fe_2O_3, MgO, NiO and LOI (Figures 4a, b).

The UMIA [2] is different in the saprolite and ferruginous saprolite of the two cores. Profile 84 presents a regular succession of horizons characteristic of this type of laterite: oxide zone (UMIA=51), ferruginous saprolite (UMIA=39), saprolite (UMIA=22 to 40) and slightly weathered serpentinized bedrock (UMIA=15). The oxide zone is underdeveloped in the two cores, and the ferruginous saprolite horizon (UMIA=41 to 60) is more developed in core 83 with UMIA from 30 to 40. The saprolite horizons are similar in both profiles, but the content in NiO is higher in 84.

 doi:10.20944/preprints202308.0428.v1

5.2. Trioctahedral versus dioctahedral smectites

Type I smectite, from the saprolite horizon, is trioctahedral in character (Supplementary Material Table S2) with a ratio between tetrahedral and octahedral cations of 1.26, near the ideal value of 1.33, and an octahedral occupancy of 2.99, where Mg is dominant. Its composition is intermediate between a saponite and nontronite, and presents two types of textures: as random curved platelets filling cores of dissolved olivine (Figure 6b), and as pseudomorphs of pyroxene (Figure 6c). Octahedral occupation of Ni is < 0.2.

Type II smectite is dioctahedral, close to nontronite, with a tetrahedral/octahedral ratio equal to 1.92, and an octahedral occupancy of 2.08, where Fe^{3+} is dominant (Supplementary Material Table S2). This smectite appears in the ferruginous saprolite, very often as pseudomorphs of type II serpentine (Figure 6f). Occupancy of Ni is under 0.14. It appears that, towards the top, smectites become more stable by increasing their dioctahedral character. All smectites are very deficient in interlaminar cations (Ca and Na), suggesting that they could be mixed with kerolite. Smectites in samples with less goethite (and more magnetite/maghemite) (Supplementary Material Table S4) have higher Ni contents, which attains its maximum occupancy in the structure in the central part of the saprolite in core 84 (samples 84-7,6,5) (Figure 4b). The compositional variation of the smectites of San Felipe is similar to those of Murrin Murrin, described by [64]. Similarly, a transition towards the top from a trioctahedral to a more dioctahedral coincides with the description for different weathering profiles developed in ultramafic rocks [23,65,66].

5.3. Type I serpentine versus type II serpentine

Two types of serpentine can also be distinguished. Type I, with low Ni and with excellent crystallinity, only appears surrounding pseudomorphed olivine grains in sample 84-12 (Figure 6b). The structural formula calculated by TEM in lizardite particles from this sample is $(Mg_{2.69}Fe_{0.15}Ni_{0.01}Si_{2.02}O_5(OH)_4$ [37]. Type II is a different generation of serpentine, less crystalline and with higher Ni contents (Supplementary Material Table S3), which coexists spatially with type II smectite in both profiles. The mean structural formula for type II serpentine in sample 84-6 $(Mg_{1.97}Fe_{0.30}Ni_{0.14}Al_{0.13})Si_{2.09}O_5(OH)_4$, can be considered a solid solution of the three end-members lizardite, Fe_2SiO_5 $(OH)_4$, and népouite, the latter two components being less soluble and stabilizing the serpentine as pore water becomes more acidic and oxidizing. As with smectites, Fe^{3+} in serpentines increases towards the top. Type II serpentine may be the result of topotactic reactions that incorporate Ni and Fe in type I serpentine. For a complete discussion about solubility and stability of Mg-Fe-Ni-serpentines in laterites see [44].

Serpentine in profiles 83 and 84 includes the crystalline form of lizardite, which is dominant, together with fewer chrysotile in core 84. Most lizardite in the weathered peridotite is well crystallized showing narrow diffraction peaks (Figure 11c). The mean crystallite size calculated in the refinement of the PXRD is estimated to be around 40 nm. In addition, a small incipient less crystalline fraction of lizardite with a crystallite size of 8 nm is also observed.

5.4. XRPD interpretation of smectite (versus kerolite-type structures)

The quantification of mineral phases by XRPD raises several relevant issues regarding the distribution of Ni among the different phyllosilicates present in the samples. The phyllosilicates *sensu lato* encountered in XRPD profiles are smectite, a kerolite-type structure, serpentine (lizardite plus chrysotile), and chlorite. The identification and quantification of the latter two through XRPD is simple since both phases are well crystallized. However, identifying and estimating the amount of smectite and/or a kerolite-type structure is more problematic because part of their diffractograms would coincide. Previous works [58,62] have shown that kerolite, and its Ni equivalent pimelite, occurs generally in association with weathered ultramafic rocks as coatings or vein infillings at the bottom of weathering profiles in association with serpentine. [22] have found that smectite and kerolite were almost always intimately associated in Ni-laterites resulting from weathering of pyroxenites. Kerolite is often a ubiquitous poorly crystalline phase present in saprolites that can be

 doi:10.20944/preprints202308.0428.v1

associated either to a smectite or to talc. Provided the lack of reliable published crystal structures of trioctahedral and dioctahedral smectites, they can only be included with precaution in the calculation of a powder diffraction file. On the contrary, kerolite profile can be fitted well using the crystal structure of talc as shown in Figure 11. As a result, it cannot be ascertained by XRPD which contribution to the turbostratic profile corresponds to smectite and which to kerolite, or even to a modified/dehydrated smectite, which could be an artifact produced during the powdering of the samples. The relative amount of smectite can be estimated by the 001 reflection, which is more important in the bottom of 83 than in 84. It is worth noting that the encountered smectites have a very low content of interlaminar cations, Na^{+} and Ca^{2+}, so that their composition is close to a 2:1 dioctahedral or trioctahedral phyllosilicate. In particular, in the saprolite horizon of core 84, type I smectites, with low Fe content, approximate the composition of a talc-like structure.

5.5. Mineral variations and weathering process across the lateritic profiles

Olivine and pyroxene relicts are absent in both profiles. The bulk composition of sample 84-12 (Supplementary Material Table S1) allows an approximate estimation of the mineral composition of the parent rock before serpentinization (and alteration of pyroxene). Assuming that only few Mg has been lost by dissolution of a small amount of olivine, the Si/(Mg+Fe) molar ratio obtained from XRF is compatible with a peridotite rich in orthopyroxene (~60 % molar). Complete serpentinization of olivine would consume an equivalent amount of orthopyroxene (in molar units), leaving an important fraction of total pyroxene (~46 % molar). Accordingly, the parent rock can be classified as an orthopyroxene-rich harzburgite. This remnant pyroxene is the base for the formation of new hydrated phases (smectite, kerolite). As weathering proceeds, part of the initial (hydrothermal, oceanic) serpentine (type I serpentine) will change its composition incorporating Fe and Ni and become less soluble, while the remainder serpentine will be dissolved incongruently, leaving some silica retained [44]. This silica is needed for the formation of smectite, and possibly chlorite. In profile 84, Mg is lost progressively, from the bottom to the top, and the Mg discontinuity between the saprolite horizon and the oxide zone is less sharp compared with other lateritic profiles worldwide [19,67]. From the bottom to the top, the profile is enriched in the less soluble elements, Fe, Al and Cr. Excess silica forms quartz, while Fe forms goethite, hematite and maghemite. Gibbsite has not been observed so that it is concluded that Al has been incorporated in the iron oxides and oxyhydroxides. Indeed, goethite in top of 83 and 84 contains 10% mole fraction of diaspore AlOOH component. In hematite from the same horizons the mole fraction of corundum is only 5%.

Interstratified Ni clays were not observed neither in San Felipe, (Figure 8) nor in Western Australia [23]. Chlorite, formed as a secondary mineral, was identified in the saprolite of core 83 and in the ferruginous saprolite of both cores (Supplementary Material Table S4 and Figure 5g).

The profile 84 follows a regular model of formation of Ni laterites in moderately tropical humid climates with marked dry seasons (1500 mm rainfall and 27^{0}C), after exposition to the surface for some million years [1,7,11]. Initial weathering of serpentinized ultramafic rocks dissolves part of type I serpentine and incipient smectite pseudomorphing pyroxene, leaching Mg and, to a lesser extent, Si, downwards. Magnetite is oxidized to maghemite or to goethite. The latter is able to retain Ni somehow, so that this element is not leached immediately [68]. Goethite is the main mineral in the oxide zone. It may contain up to 2.7 wt.% NiO [30]. Serpentine and smectite incorporate Fe^{3+} and Ni that substitute Mg in the octahedral positions of both minerals. In this process, the more soluble Mg hydrous silicate component is being substituted by the less soluble, which incorporates more Fe^{3+} and Ni, so that the more soluble (more Mg, less Fe^{3+} and Ni) appears below the less soluble in the profile. The rate at which the Ni retained initially by goethite is liberated, compared with the rate of its capture by the new hydrous silicates formed downwards (incipient smectite → smectite I → smectite II; serpentine I → serpentine II) determines the content of Ni along the entire profile.

The bottom of profile 84 is poor in NiO (Supplementary Material Table S1, 0.33 wt.%, sample 84-12), and similar to the Ni content in peridotites [19]. Supergene enrichment has not yet taken place significantly, serpentines being formed in pre-weathering conditions. In the saprolite horizon, 85% of Ni is contained in type I smectite, and only 15% in serpentine. Serpentine (Supplementary Material

 doi:10.20944/preprints202308.0428.v1

Table S3) is enriched in Ni with respect to the same mineral at the base of the profile, however its amount decreases towards the top, so that its contribution to nickel content near the top is only about 5 wt.%. The sample 84-12 represents the slightly weathered, serpentinized peridotite that, nevertheless, has been deeply altered in hydrothermal (oceanic) conditions, prior to weathering. Olivine and pyroxene have completely been transformed to serpentine and smectite and/or kerolite before weathering. The initial transformation of enstatite to smectite is favored by the crystallographic similarities and the chain structure of the former, along its cleavage and exsolution planes [22,64], but needs some afford of silica, that possibly comes from incongruent dissolution of part of the olivine.

The anomalous increase of serpentine and magnetite/maghemite or goethite near the top in both profiles (samples 83-6 and 84-4) may be due to floating blocks of bedrock that have been frequently detected by GPR (Ground Penetrating Radar) in the San Felipe formation [30]. This is corroborated by correlation coefficients between serpentine and magnetite/maghemite or goethite for profiles 83 and 84, of 0.4 and 0.6, respectively.

It is worth noting that profile 84, from the border of the plateau, would represent an undisturbed profile that corresponds to stationary development of regular horizons in the given lithologic and climatic conditions, and an active drainage. On the contrary, profile 83, from the center of the plateau, presents fragmented microcrystalline quartz vein infillings and displays evidences of reworking along the profile. This would be a result of complex, not well understood episodes of precipitation of silica forming crusts, and collapse of part of the profile and further replenishment downwards produced by active tectonics during the Pliocene [30].

5.6. Comparison between smectites from lateritic profiles worldwide

The Supplementary Material Table S5 displays selected structural formulae of Ni-bearing smectites from Ni-laterite profiles worldwide. There are many differences between smectites based on: i) the total layer charge and the distribution of this charge between the octahedral and the tetrahedral sheets; ii) the Ni, Mg and Fe content in the octahedral position; iii) the origin, formed after olivine, or (ortho- and clino-) pyroxene or lizardite. These differences can be explained by the position of smectites in the lateritic profiles, and above all, the parent rock, topography, and climate.

The Ni-smectite from the pyroxenite of Niquelândia (Brazil) [64] is the richest in Ni (2.14 hafu and 2.71 cations in octahedral position), and other two with remarkable Ni are those of Tagaung (Myanmar), and Falcondo (Dominican Republic) [24,54], the sum of the octahedral cations being 1.8 and 1.75 hafu, and 2.71 or 3.06 cations in the octahedral position, respectively (Supplementary Material Table S5), confirming the trioctahedral character. Another smectite with dominant Ni in the octahedral position (1.03 hafu) is the one from the lower saprolite of Tagaung [54], but in this case, the sum of the octahedral cations is 2.43 (intermediate between trioctahedral and dioctahedral). Iron in the octahedral position is dominant in six smectites, two from Myanmar, three from Western Australia and one from Cuba [37,51,54], the sum of the octahedral cations being between 2.01 and 2.27 hafu (Supplementary Material Table S5), confirming the dioctahedral character and a slight octahedral over-occupancy. Finally, Mg is the main octahedral cation in five smectites, two from Western Ivory Coast [49], two from Western Australia [23,51] and two from Cuba.[37] Four of them yield an octahedral cation sum between 3.06 and 2.86 hafu (trioctahedral character), and the other one is 2.26 hafu (dioctahedral character) (Supplementary Material Table S5). The smectite with highest Mg in the octahedral position (1.82 hafu, 3.06 total occupancy, trioctahedral) is from a serpentinized dunite and formed after olivine.

The highest Al in the tetrahedral position is 0.71 hafu in the trioctahedral smectite in the transition layer in Western Ivory Coast [49]. Aluminum in the tetrahedral position is only absent in one sample in the lower saprolite layer in Myanmar [54], with non-deficit charge in the tetrahedral position. Iron is present in five samples in tetrahedral position, three of them are the richest in Ni in the octahedral position (Brazil, Myanmar, Dominican Republic) [24,54,64].

 doi:10.20944/preprints202308.0428.v1

Serpentine was detected by X-ray diffraction together with smectite in ten samples [24,37,49,54]. Only in Murrin Murrin (serpentinized peridotite) and Wingellina (gabbro) in Western Australia and in Niquelândia (pyroxenite) in Brazil, serpentine was not reported [23,51,66].

6. Conclusions

The original mineral composition of the bedrock in the San Felipe Ni-laterite deposit is estimated to have a molar ratio between enstatite and forsterite of about 3. This mineral composition greatly influences the mineral evolution during weathering as well as the degree of supergene enrichment in Ni. In profile 83 the average of NiO is 0.87 wt.%, while it is 1.79 wt.% in profile 84. Values of CoO are respectively 0.03 and 0.06 wt.%.

Smectite and serpentine evolve in parallel towards the top incorporating the less soluble elements Fe (as Fe^{3+}), Al and Ni. For smectites, this evolution represents a transformation from trioctahedral to dioctahedral character. Even if serpentine doubles the NiO content of smectite (~3.2 and ~1.5 wt.%, respectively), smectite is much more abundant in the saprolite, so that this mineral contains about 80 % of the total Ni, the remainder being located in serpentine. In the ferruginous saprolite, the Ni content in smectite is even higher.

Nevertheless, taking into account the amount of smectite and serpentine, their Ni content, and the size of the plateau, the San Felipe deposit could be considered an attractive resource for Ni, comparable to other large Ni-laterite deposits in the Caribbean, such as Moa Bay, Cerro Matoso and Falcondo.

Interlaminar cation content in smectites is very low, suggesting that part of the X-ray turbostratic profile observed is in fact an intermediate structure between kerolite and a collapsed smectite.

Profile 84 displays a regular succession of horizons that is currently interpreted by a model of progressive enrichment of phyllosilicates in less soluble elements. This regular succession is disrupted in profile 83 by a concentration of silica rich material, mainly fragments of cryptocrystalline quartz, which probably reveals a complex succession of events of collapse and replenishing of the area where the laterite was developed. The high content of free silica in this profile greatly reduces its NiO content.

Supplementary Materials: The following supporting information can be downloaded at the website of this paper posted on Preprints.org, Table S1: Major elements in wt.% of cores 83 and 84 (LOD = below limit of detection).; Table S2: Representative EMPA analyses (in weight percent) and structural formulae (in half-atoms per formula unit -hafu-, based on 11 oxygens) of smectite. Analyses 84-02-1, 84-02-2, 84-02-3 and 84-02-4 are from type II smectite in ferruginous saprolite (sample 84-02); 83-23-5, 83-23-6, 83-23-7 and 83-07-8 are from smectite type II in ferruginous saprolite (sample 83-23); 84-09-9 and 84-09-10 are from smectite type I from olivine, and 84-09-11 and 84-09-12 are from smectite type I from pyroxene in weathered peridotite/saprolite (sample 84-09).; Table S3: Representative EMPA analyses (in weight percent) and structural formulae (in half-atoms per formula unit, based on 7 oxygens) of serpentine II from sample 84-07 (saprolite horizon). The point analyses 20, 26, 27, 28 and 30 are in Figure 7., Table S4: Quantitative determination (in wt.%) of the mineral phases present in the selected samples, obtained by Rietveld refinement of XRPD. Legend: Mag = magnetite, Mgh = maghemite.; Table S5: Structural formulae of Ni-smectite from various localities worldwide, ordered by Ni content in the octahedral position (hafu based on 11 oxygens).

Author Contributions: Conceptualization, E.T., S.G. and J.A.P.; methodology, E.T., S.G., C.V.B. and J.A.P.; software, E.T., S.G. C.V.B. and G.K.; validation, E.T., S.G., C.V.B. and J.A.P.; formal analysis, E.T., S.G. and C.V.B.; investigation, E.T., S.G., C.V.B., A.C.R., K.N.C., G.K., J.A.P.; data curation, E.T., S.G. and C.V.B.; writing—original draft preparation, E.T. and S.G.; writing—review and editing, E.T., S.G., C.V.B., A.C.R., K.N.C., G.K., J.A.P.; supervision, J.A.P.; project administration, J.A.P.; funding acquisition, J.A.P. All authors have read and agreed to the published version of the manuscript.

Funding: This research was funded by Agència de Gestió d'Ajuts Universitaris i de Recerca de Catalunya, grant number 2021 SGR 00239; and by the Ministerio de Ciencia e Innovación (MCIN) and the Agencia Estatal de Investigación (AEI) of Spain, grant number PID2019-105625RB-C21. This research has been financially supported byFEDER Funds, the Spanish projects CGL2009-10924 and CGL2012-36263.

Acknowledgments: The Authors would like to thank Eng. Enrique Piñero for his inestimable support during fieldwork.

Conflicts of Interest: The authors declare no conflict of interest.

References

1. Freyssinet, Ph.; Butt, C.R.M.; Morris, R.C. Ore-forming processes related to lateritic weathering. *Econ Geol 100th Anniv* **2005,** 681–722. https://doi. org/10.5382/AV100.21
2. Aiglsperger, T.; Proenza, J.A.; Lewis, J.F,; Labrador, M.; Svojtka, M.; Rojas-Purón, A.; Longo, F.; Ďurišová, J. Critical metals (REE, Sc, PGE) in Ni laterites from Cuba and the Dominican Republic. *Ore Geol Rev* **2016,** 73, 127–147. https://doi.org/10.1016/j. oregeorev.2015.10.010
3. Chassé, M.; Griffin, W.L.; Reilly, S.Y.O.; Calas, G. Scandium speciation in a world-class lateritic deposit: *Geochemical Perspectives Letters* **2017**, 3, 105–114. https://doi.org/10.7185/geochemlet.1711
4. Dalvi, A.D.; Gordon Bacon, W.; Osborne, R.C. The past and the future of nickel laterites. *PDAC Int. Convention* **2004**, Toronto, p 27.
5. McRae, M.E. US Geological Survey, Mineral Commodity Summaries 2022 - Nickel. https://pubs.usgs.gov/periodicals/mcs2022/mcs2022-nickel.pdf
6. Freyssinet, Ph.; Butt, C.R.M.; Morris, R.C. Ore-forming processes related to lateritic weathering. *Econ Geol 100th Anniv* **2005,** 681–722. https://doi. org/10.5382/AV100.21
7. Golightly, J.P. Nickeliferous laterite deposits. *Econ Geol 75th Anniv* **1981**, 710–735. https://doi.org/10.5382/AV75.18
8. Gleeson, S.A.; Butt, C.R.; Elias, M. Nickel laterites: a review. *SEG Newsletter* **2003**, 54, 11–18.
9. Gaudin, A.; Decarreau, A.; Noack, Y.; Grauby, O. Clay mineralogy of the nickel laterite ore developed from serpentinised peridotites at Murrin Murrin, Western Australia. *Australian J Earth Sci* **2005**, 52,231–241. https://doi.org/10.1080/08120090500139406
10. Thorne, R.L.; Roberts, S.; Herrington, R. Climate change and the formation of nickel laterite deposits. *Geology* **2012**, 40, 331–334. https://doi.org/10.1130/G32549.1
11. Butt, C.R.M.; Cluzel, D. Nickel laterite ore deposits: Weathered serpentinites. *Elements* **2013**, 9, 123–128. https://doi.org/10.2113/gselements.9.2.123
12. Maurizot, P.; Sevin, B.; Iseppi, M.; Giband, T. Nickel-bearing laterite deposits in accretionary context and the case of New Caledonia: from the large-scale structure of earth to our everyday appliances. *GSA Today* **2019**, 29, 4–10. https://doi.org/10.1130/GSATG364A.1
13. Butt, C. R. M. Nickel Laterites and Bauxites: A Summary of Observations Made During an Overseas Trip in 1974. CSIRO Division of Mineralogy, Minerals Research Laboratories **1975**.
14. Golightly, J.P. Progress in understanding the evolution of nickel laterites. *Econ Geol Spec Pub* **2010**, 15, 451–485. https://doi.org/10.5382/SP.15.2.07
15. Brand, N.W.; Butt, C.R.M.; Elias, M. Nickel laterites: classification and features. *AGSO J Australian Geol Geoph* **1998**, 17, 81–88.
16. Wells M.A.; Ramanaidou, E.R.; Verrall, M.; Tessarolo, C. Mineralogy and crystal chemistry of garnierites in the Goro lateritic nickel deposit, New Caledonia. *Eur J Miner* **2009**, 21, 467–483. https://doi.org/10.1127/0935-1221/2009/0021-1910
17. Villanova-de-Benavent, C.; Proenza, J.A.; Galí, S.; García-Casco, A.; Tauler, E.;Lewis, J.F.; Longo, F. Garnierites and garnierites: textures, mineralogy and geochemistry of garnierites in the Falcondo Ni-laterite deposit, Dominican Republic. *Ore Geol Rev* **2014**, 58, 91–109. https://doi.org/10.1016/j. oregeorev.2013.10.008
18. Cathelineau, M.; Quesnel, B.; Gautier, P.; Boulvais, P.; Couteau, C.; Drouillet, M.Nickel dispersion and enrichment at the bottom of the regolith: formation of pimelite target-like ores in rock block joints (Koniambo Ni deposit, New Caledonia). *Mineral Deposita* **2016**, 51, 271–282. https://doi.org/10.1007/s00126-015-0607-y
19. Tupaz, C.A.J.; Watanabe, Y.; Sanematsu, K.; Echigo, T. Mineralogy and Geochemistry of the Berong Ni-Co laterite Deposit, Palawan, Philippines; *Ore Geol Rev* **2020**, 125:103686. https://doi. Org /10. 1016/j.oregeorev.2020.103686
20. Lambiv Dzemua, G.; Gleeson, S.A.; Schofield P.F. Mineralogical characterization of the Nkamouna Co–Mn laterite ore, southeast Cameroon: *Miner Deposita* **2013**, 48, 155-171. https://doi.org/10.1007/s00126-012-0426-3

21. Nahon, D.B.; Paquet, H.; Delvigne, J. Lateritic weathering of ultramafic rocks and the concentration of nickel in the Western Ivory Coast. *Econ Geol* **1982**, 77, 1159–1175
22. Colin, F.; Noack, Y.; Trescases, J.J.; Nahon, D. L'alteration latéritique débutante des pyroxenites de Jacuba, Niquelândia, Brésil. *Clay Miner* **1985**, 20, 93–113. https:// doi. org/10.1180/claymin.1985.020.1.08
23. Putzolu, F.; Abad, I.; Balassone, G.; Boni, M.; Mondillo, N. Ni-bearing smectites in the Wingellina laterite deposit (Western Australia) at nanoscale: TEM-HRTEM evidences of the formation mechanisms. *Appl Clay Sci* **2020,** 196,105753. https://doi. Org /10. 1016/j.clay.2020.105753
24. Tauler, E.; Lewis, J.F.; Villanova-de-Benavent, C.; Aiglsperger, T.; Proenza, J.A.;Domènech, C.; Gallardo, C.; Longo, F.; Galí, S. Discovery of Ni-smectite-rich saprolite at Loma Ortega, Falcondo mining district (Dominican Republic): geochemistry and mineralogy of an unusual case of "hybrid hydrous Mg silicate–clay silicate" type Ni-laterite. *Miner Deposita* **2017**, 52, 1011–1030. https://doi.org/10.1007/s00126-017-0750-8
25. Nelson, C.E.; Proenza, J.A.; Lewis, J.F.; López-Kramer, J. The metallogenic evolution of the Greater Antilles. *Geol Acta* **2011**, 9, 229–264. https://doi.org/10.1344/105.000001741
26. Chang-Rodríguez, A.; Rojas, A. Fases minerales portadoras de níquel presentes en el horizonte saprolítico del yacimiento San Felipe. *Minería & Geología* **2015**, 31(4), 1-18.
27. Chang-Rodríguez, A.; Tauler, E.; Lavaut, W.; Rojás-Purón, A.L.; Proenza, J.A. Caracterización geoquímica del perfil litológico del yacimiento laterítico de níquel "San Felipe", Camagüey, Cuba". *Revista Ciencias de la Tierra y del Espacio* **2015**, 16(2), 9-22.
28. Chang-Rodríguez, A.; Tauler, E.; Proenza, J.A.; Rojas-Purón, A.L. Mineralogía del yacimiento laterítico de níquel San Felipe. *Minería & Geología* **2016**, 32 (1), 28-47.
29. Cobas-Botey, R.M. Caracterización geológica de las lateritas en diferentes regiones metalogénicas: comparación de los yacimientos San Felipe y Piloto. *Minería & Geología* **2016**, 32(1), 48-59.
30. Cobas-Botey, R.M.; Formell-Cortina, F.; Leyva-Rodríguez, C. Modelo geológico descriptivo del yacimiento laterítico San Felipe, Camagüey, Cuba. *Minería & Geología* **2017**, 33(3), 251-264.
31. Iturralde-Vinent, M.A.; Garcia-Casco, A.; Rojas-Agramonte, Y.; Proenza, J.A.; Murphy, J.B.; Stern, R.G. The geology of Cuba: a brief overview and syn thesis **2016**. GSA Today 26 (10), 4-10.
32. Rojas-Agramonte, Y.; Garcia-Casco, A.; Kemp, A.; Kröner, A.; Proenza, J.A.; Lázaro, C.; Liu, D. Recycling and transport of continental material through the mantle wedge above subduction zones: a Caribbean example. *Earth and Planetary Science Letters* **2016**,436, 93-107.
33. Iturralde-Vinent, M. Introduction to Cuban geology and geophysics. Ofiolitas y Arcos Volcánicos de Cuba. Miami, Florida, *International Geological Correlation Programme* **1996**, Project 364, 3-35.
34. Lewis, J.F.; Draper, G.; Proenza, J.A.; Espaillat, J.; Jiménez, J. Ophiolite-related ultramafic rocks (serpentinites) in the Caribbean region: A review of their occurrence, composition, origin, emplacement and nickel laterite soils. *Geol. Acta* **2006**, 4, 237–263.
35. Farr,T.G.; Rosen,P.A.; Caro, E.; Crippen, R.; Duren, R.; Hensley, S.; Kobrick, M.; Paller, M.; Rodriguez, E.; Roth, L.; Seal, D.; Shaffer, S.; Shimada, J.; Umland, J.; Werner, M.; Oskin, M.; Burbank, D.; Alsdorf, D. The Shuttle Radar Topography Mission, *Geophys* **2007**, 45, RG2004, https://doi.org/10.1029/2005RG000183
36. Kelso, N. V.; Patterson, T. Introducing natural earth data - naturalearthdata.com, *Geographia Technica* **2010**, 5(82-89), 25.
37. Gallardo, T.; Tauler, E.; Garcia-Romero, E.; Proenza, J.A.; Suarez-Barrrrios, M.; Chang, A. Caracterización Mineralógica de las Esmetitas Niquelíferas del Yacimiento de San Felipe (Camagüey, Cuba). *Macla* **2011**,15, 89-90.
38. Lázaro, C.; García-Casco, A.; Blanco-Quintero, I.F.; Rojas- Agramonte, Y.; Corsini, M.; Proenza, J.A. Did the Turonian–Coniacian plume pulse trigger subduction initiation in the Northern Caribbean? Constraints from 40Ar/39Ar dating of the Moa-Baracoa metamorphic sole (eastern Cuba). *International Geology Review* **2015**, 57, 919-942. https://doi. org/10.1080/00206814.2014.924037
39. Young, R.A. The Rietveld Method. International Union of Crystallography; Oxford University Press: Oxford, UK, 1993; p.298. ISBN 0198555776
40. TOPAS. General Profile and Structure Analysis Software for Powder Diffraction Data, version 4.2, Bruker AXS Gmbh, Karlsruhe, Germany, 2009.
41. Pouchou, J.L.; Pichoir, F. Electron probe x-ray microanalysis applied to thin surface films and stratified specimens. Scanning Microscopy Supplement 7, **1993**, 167-189.

42. Decarreau, A.; Colin, F.; Herbillon, A.; Manaceau, A.; Nahon, D.; Paquet, H.; Trauth-Badaud, D.; Trescases, J.J. Domain segregation in Ni-Fe-Mg smectites. *Clays Clay Miner* **1987**, 35, 1–10. https://doi. Org /10. 1346/ CCMN. 1987. 03501 01
43. Roque-Rosell, J.; Villanova-de-Benavent, C.; Proenza, J.A. The accumulation of Ni in serpentines and garnierites from the Falcondo Ni-laterite deposit (Dominican Republic) elucidated by means of μXAS. *Geochim Cosmochim Acta* **2017**, 198, 48–69. https://doi. Org /10. 1016/j. gca. 2016. 11. 004
44. Villanova-de-Benavent, C.; Domènech, C.; Tauler, E.; Galí, S.; Tassara, S.; Proenza, J.A. Fe–Ni-bearing serpentines from the saprolite horizon of Caribbean Ni-laterite deposits: New insights from thermodynamic calculations. *Miner Deposita* **2017**, 52, 979–992. https://doi.org/10.1007/s00126-016-0683-7
45. Guggenheim, S.; Adams, J. M.; Bain, D. C.; Bergaya, F.; Brigatti, M. F.; Drits, V. A.; Formoso, M. L. L.; Galán, E.; Kogure, T.; Stanjek, H. Summary of recommendations of nomenclature committees relevant to clay mineralogy: report of the Association Internationale pour l'etude des Argiles, nomenclature committee for 2006. *Clay Minerals* **2006**, 41, 863–877. https://doi.org/10.1180/0009855064140225
46. Bosio, N.J.; Hurst, V.J.; Smith, R.L. Nickeliferous nontronite, a 15 Å garnierite, at Niquelândia, Goiás, Brazil. *Clays Clay Miner* **1975**, 23, 400–403.
47. Brindley, G.W.; de Souza, J.V. Nickel containing montmorillonites and chlorites from Brazil, with remarks on schuchardtite. *Mineral Mag* **1975**, 40, 141–152.
48. Nahon, D.B.; Colin, F. Chemical weathering of orthopyroxenes under lateritic conditions. *Am J Sci* **1982**, 282, 1232–1243. https://doi.org/10.2475/ajs.282.8.1232
49. Nahon, D.B.; Colin F.; Tardy, Y. Formation and distribution of Mg, Fe, Mn-smectites in the first stages of the lateritic weathering of forsterite and tephroite. *Clay Miner* **1982**, 17, 339–348. https://doi.org/10.1180/claymin.1982.017.3.06
50. Pelletier B (1996) Serpentines in nickel silicate ore from New Caledonia. Australasian Institute of Mining and Metallurgy publication series—nickel conference Bmineral to market^, Kalgoorlie. Western Australia 6(96):197–205.
51. Gaudin, A.; Grauby, O.; Noack, Y.; Decarreau, A.; Petit, S. Accurate crystal chemistry of ferric smectites from the lateritic nickel ore of Murrin Murrin (Western Australia). I XRD and multi-scale chemical approaches. *Clay Miner* **2004**, 39, 301–315.https://doi.org/10.1180/0009855043930136
52. Gleeson, S.A.; Herrington, R.J.; Durango, J.; Velásquez, C.A.; Koll, G.The mineralogy and geochemistry of the Cerro Matoso S.A. Nilaterite deposit, Montelíbano, Colombia. *Econ Geol* **2004,** 99, 1197–1213. https://doi.org/10.2113/gsecongeo.99.6.1197
53. Suárez, S.; Nieto, F.; Velasco, F.; Martín, F.J. Serpentine and chlorite as effective Ni-Cu sinks during weathering of the Aguablanca sulphide deposit (SW Spain). TEM evidence for metal-retention mechanisms in sheet silicates. *Eur J Miner* **2011**, 23, 179–196. https://doi.org/10.1127/0935-1221/2011/0023-2084
54. Murofushi, A.; Otake, T.; Sanematsu, K.; Zay Ya, K.; Ito, A.; Kikuchi, R.; Sato, T. Mineralogical evolution of a weathering profile in the Tagaung Taung Ni laterite deposit: significance of smectite in the formation of high-grade Ni ore in Myanmar. *Min Deposita* **2022**, 57, 1107–1122. https://doi.org/10.1007/s00126-021-01089-6
55. Velde, B. Clay minerals: a physico-chemical explanation of their occurrence **1985**. Amsterdam, Elsevier, p 427. ISBN : 0444424237 (U.S.)
56. Chen, T.T.; Dutrizac, J.E.; Krause, E.; Osborne, R. Mineralogical characterization of nickel laterites from New Caledonia and Indonesia. Int Laterite Nickel Symposium **2004**, 79–99.
57. Golightly, J.P.; Arancibia, O.N.The chemical composition and infrared spectrum of nickel- and iron-substituted serpentine form a nickeliferous laterite profile, Soroako, Indonesia. *Can Mineral* **1979**, 17, 719–728
58. Brindley, G.W.; Bish, D.L.; Wan, Hsien-Ming. The nature of kerolite, its relation to talc and stevensite. *Min Magazine* **1977**, 41, 443-452.
59. Hillier, S. Accurate quantitative analysis of clay and other minerals in sandstones by XRD: comparison of a Rietveld and a reference intensity ratio (RIR) method and the importance of sample preparation. *Clay Minerals* **2000**, 35, 291-302. https://doi.org/10.1180/000985500546666
60. Srodon, J. Identification and Quantitative Analysis of Clay Minerals. Developments in Clay Science 2013. https://doi.org/10.1016/B978-0-08-098259-5.00004-4

61. Reynolds, R.C. Principles and techniques of quantitative analysis of clay minerals by X-ray powder diffraction. Quantitative Mineral Analysis of clays (D.R. Pevear and F.A. Mumpton, editors) CMS 1989, pp 437.
62. Brindley, G.W.; Brown, G. Crystal structures of clay minerals and their X-ray identification 1980, Mineralogical Society, pp-495. ISBN 0 903056 08 9
63. Suquet, H.; Malard, C.; Copin, E.; Pezerat, H. Variation du parameter b et de la distance basale d 001 dans une serie de saponites à charge roissante: I. Ëtats hydrates. II Ëtats "zero couche". *Clay Miner* **1981**, 16, 53-67, 181-193.
64. Colin, F.; Nahon, D.; Trescases, J.J.; Melfi, A.J. Lateritic weathering ofpyroxenites at Niquelandia, Goias, Brazil: the supergene behaviour of nickel. *Econ Geol* **1990**, 85, 1010–1023. https://doi.org/10.2113/gsecongeo.85.5.1010
65. Paquet H., Duplay J., Nahon D., Tardy Y. & Millot G. Analyses chimiques de particules isole´es dans les populations de mine´raux argileux. Passage des smectites magnésiennes trioctaédriques aux smectites ferrifères dioctaédriques au cours de l'altération des roches ultrabasiques. Comptes Rendus de l'Académie des Sciences II **1983**, 296, 699-704.
66. Colin, F.; Nahon, D.; Trescases, J.J.; Melfi, A.J. Lateritic weathering ofpyroxenites at Niquelandia, Goias, Brazil: the supergene behaviour of nickel. *Econ Geol* **1990**, 85, 1010–1023. https://doi.org/10.2113/gsecongeo.85.5.1010
67. Aquino, K.A.; Arcilla, C.A.; Schardt, C.;Tupaz, C.A.J. Mineralogical and geochemical characterization of the Sta. Cruz Nickel laterite deposit, Zambales, Philippines. Minerals 2022, 12, 305. https://doi.org/10.3390/min12030305
68. Domènech, C.; Galí, S.; Villanova-de-Benavent, C.; Soler, J.M.; Proenza, J.A. Reactive transport model of the formation of oxide-type Ni-laterite profiles (Punta Gorda, Moa Bay, Cuba). *Miner. Dep*. **2017**, 52, 993–1010. https://doi.org/10.1007s00126-017-0713-0